Stability Enhancement for IBRs Operating in Weak Grids Through Proper Coordination and Control

Ratik Mittal, *Student Member, IEEE,* Zhixin Miao, *Senior Member, IEEE,* Lingling Fan, *Fellow, IEEE*

***Abstract*—In this work, a coordination and control scheme for multiple inverter-based resources (IBRs) operating in weak grids is proposed to improve stability margin close to the steady-state power transfer limit. The scheme can achieve further stability enhancement even with well-designed individual IBR's control. The key philosophy is to have one set of IBRs providing modulated reactive current that can mitigate weak grid oscillations. This philosophy is realized through coordination or implementing a voltage feedback control to modulate the reactive current order of a set of IBRs. To test its robustness, three testbeds experiencing 3-Hz to 7-Hz oscillations are examined. Additionally, a grid-forming converter is also tested. In electromagnetic transient (EMT) computer simulation, the proposed coordination scheme is shown to improve both small-signal stability margin and large-signal stability. Furthermore, experiments have been conducted in a hardware testbed to demonstrate the efficacy of the coordination and control scheme.**

***Index Terms*—Weak grid, grid-following inverters, stability, coordination.**

I. Introduction

HIGH penetrations of IBRs have been reported in South Australia, Hawaii, Texas, Colorado, Denmark, etc. [1] As a consequence, weak grid oscillation events appeared in real-world operation [2]. In Texas, an ERCOT wind power plant experienced 4-Hz oscillations due to weak grid conditions after a line tripping event [3]. Solar photovoltaic (PV) plants in Hydro One experienced undamped 20 Hz oscillations [4]. Australian Energy Market Operator (AEMO) witnessed 7-Hz oscillations due to insufficient grid strength in the west Murray region [5]. These oscillations were identified to be associated with multiple solar farms. More examples of real-world weak grid oscillation events are well documented in the recently published IEEE PES IBR subsynchronous oscillations task force papers [6], [7].

A. State-of-the-Art Review of Weak Grid Stability Enhancement

Over the years, weak grid stability enhancement methods for grid-following voltage-sourced converter (VSC)-based IBRs have been discussed and reported. These methods can be classified into three categories: those dealing with phase-locked loops (PLLs), those dealing with inner current controls, and those dealing with outer controls.

This project is supported in part by the US Department of Energy SETO grant DE-EE-0008771.

R. Mittal, Z. Miao and L. Fan are with the Department of Electrical Engineering, University of South Florida, Tampa, FL, 33630 USA. Emails: {ratik, zmiao, linglingfan}@usf.edu.

It has been known that PLL introduces negative resistance in the low frequency region in the dq frame [8]. Thus, redesign PLL or tuning PLL parameters have been an active research. In [8], the authors suggest reducing the bandwidth of the PLL to weaken the effect of the negative resistance. To date, it is now widely known by the bulk grid industry that in weak grids PLL cannot be too fast since PLLs rely on voltage as input and voltage becomes sensitive to current or power injection when grid strength reduces [9]. Redesign of PLL is another option. For example, in [10], the authors propose a double-PLL-based scheme to extend the stability region of the VSC system while operating in very weak grid conditions with the short circuit ratio (SCR) at 1. The new design leads to the VSC exporting 0.9 p.u. real power when the point of common coupling (PCC) voltage is kept at 1 p.u. Instead of using voltage-based synchronization, power-based synchronization has been used in grid-forming control design and shows to achieve better stability [11]. Similarly, using the d-axis current as the input to generate angle has been proposed in [12] by R. Iravani's group and shown to boost the stability margin close to the steady-state limit. While operating at SCR of 1 with the proposed control, the VSC-HVDC is able to transfer maximum power of 1.0 p.u. with the terminal voltage at 1.0 p.u.

In the second category, recent research indicates that the proportional gain of the inner current control influences weak grid stability [13], [14]. [13] shows that the gain has difficulty to balance the PCC voltage response and the damping capability during weak grid conditions. Thus, the authors resolved with the restructuring of the proportional integral (PI) controller as an integral proportional (IP) controller. The redesigned current control leads to a higher stability margin for the VSC. When operating at SCR of 1, it can inject up to 1 p.u. power with the PCC voltage at 1 p.u. With the effect of the voltage feedforward unit's low-pass filter considered, the proportional gain is shown to aggravate the instability impact of PLL and make weak grid stability worse [14]. The authors indicate that co-design of the current controller and the voltage feedforward controller is necessary.

Research in the third category usually treats an inverter as a current source synchronized to the grid through a PLL. Analysis in [15] shows that the stability issue can be viewed from the perspective of a feedback system consisting of the effect of d-axis outer loop control on the d-axis current, the effect of d-axis current on the point of common coupling (PCC) bus voltage phase angle, the effect of the PLL dynamics to track this angle, the influence of the PLL output angle on the PCC voltage magnitude, and finally the influence of

voltage magnitude on real power. The weak grid stability issue can be viewed as the interaction of the real power or dc-link voltage control, the PLL, and the grid effect. Therefore, reducing the sensitivity of voltage on real power injection is a means to push the stability boundary. For example, in [16], the authors show that a VSC without outer control can operate up to the theoretic limit, while stability issue appears if the outer control is enabled. An advanced vector control is then proposed by adding four decoupling gains between the power and the voltage control loops. While operating at SCR $= 1$, the proposed control can deliver a maximum of 0.89 p.u. real power. A more simplified control was proposed in [17] by the senior authors of the current paper to reduce the high sensitivity of voltage to real power injection. Notably, a power-voltage decoupling scheme is designed and implemented to modulate the real power order by use of voltage deviation feedback. The single IBR can deliver 0.91 p.u. when $X_g = 1.1$ or SCR is 0.91. If the interaction of real power control and the PLL causes stability issue, modifying the power PI controller to compensate the phase lag introduced by the PLL can provide damping to low-frequency oscillations at weak grid conditions as demonstrated in [18]. With the suggested modification, the single grid-connected VSC was able to inject 1.0 p.u. real power when SCR is 1.1.

B. Goals and Contributions

It can be seen that several designs, e.g., [12], [17], can enhance individual IBR's stability margin close to the steady-state limit. Alternatively, parameter tuning for fixed control structures can be another option for stability enhancement. However, in some scenarios, this option may not be feasible. Take the example of the Texas 4-Hz oscillations [3], oscillations appeared upon tripping of a transmission line which led to the grid strength dropped to SCR of 2. Reducing the gain in plant-level voltage control can resolve the issue of oscillation, but this tuning slows down voltage recovery. When the grid strength is high, this set of parameters is not desired. Therefore, parameter tuning alone is not sufficient for stability enhancement in some cases.

The goal of this paper is to push a step further on stability enhancement. We investigate the following: With every IBR well designed and tuned, is there additional room for stability improvement in a multi-IBR system through IBR coordination?

To this end, we have conducted preliminary research to examine whether IBRs working identically in power and voltage control mode is the best for stability in a two-IBR system. We found that this is not necessarily true. In fact, with one IBR in voltage control mode and another in reactive power control mode, the entire system can achieve better stability. The simulation results will be presented in Section III.B.

Thus, there is room for additional improvement through coordination. In this research, an effective coordination and control scheme will be designed, implemented, and tested. With the coordination and control scheme, our tests show that the total power from the two IBRs can achieve 1.06 p.u. for a very weak grid interconnection when the SCR is 1 p.u. Since there is 0.1 p.u. resistance in the grid impedance, the steady-state limit of operation (with voltage kept at 1 p.u.) is about 1.1 p.u. It is found that the coordination scheme can effectively push IBRs to operate close to the steady-state limit.

Our contribution is three-fold.

1) We have demonstrated that proper coordination among IBRs is effective to improve stability. Identical control of IBRs is not necessarily the best. It is found that reducing the sensitivity of voltage towards reactive power or current can be achieved through IBR coordination. This finding further leads to a control design.
2) We have come up with a simple and effective control design by exploring the voltage and reactive current relationship in weak grid oscillation scenarios. Such strategy has not been explored in the state-of-the art.
3) An insightful theoretic analysis has been provided to show why such strategy can work and a thorough validation of the coordination and control scheme has been carried out in both EMT computer simulation and hardware experiments.

C. Structure of the Paper

The rest of the paper is organized as follows. Section II presents the three testbeds of multi-IBR systems. In Section III, the philosophy of coordination and the implementation in the VSC control are presented. The effect of the coordination and control scheme is also examined using a linear block diagram. Section IV presents the EMT simulation results. Section V presents the hardware testbed experiment results. Section VI concludes the paper.

II. Test Beds

The schematics of the system under study are presented in Fig. 1.

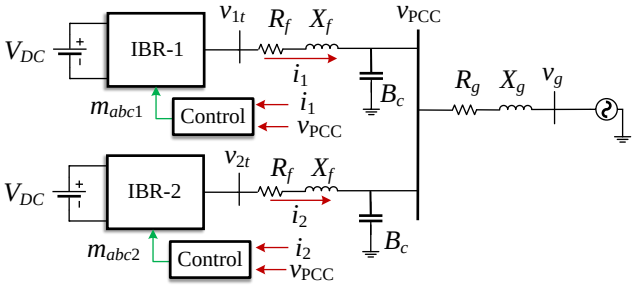

Fig. 1: Circuit topology of the two-IBR test bed.

The system consists of two three-phase DC-AC inverters connected in parallel at the PCC bus, which is further is connected to the power grid via a transmission line represented by R_g and X_g. A choke filter is connected between the terminals of the inverter. The choke filter is represented by R_f, X_f and C_f. A constant DC voltage source supplies each inverter. The AC grid is modeled as a constant voltage source ("infinite bus").

Furthermore, i_1, and i_2 are the converters current for IBR-1 and IBR-2 respectively and v_{PCC} is the PCC bus voltage.

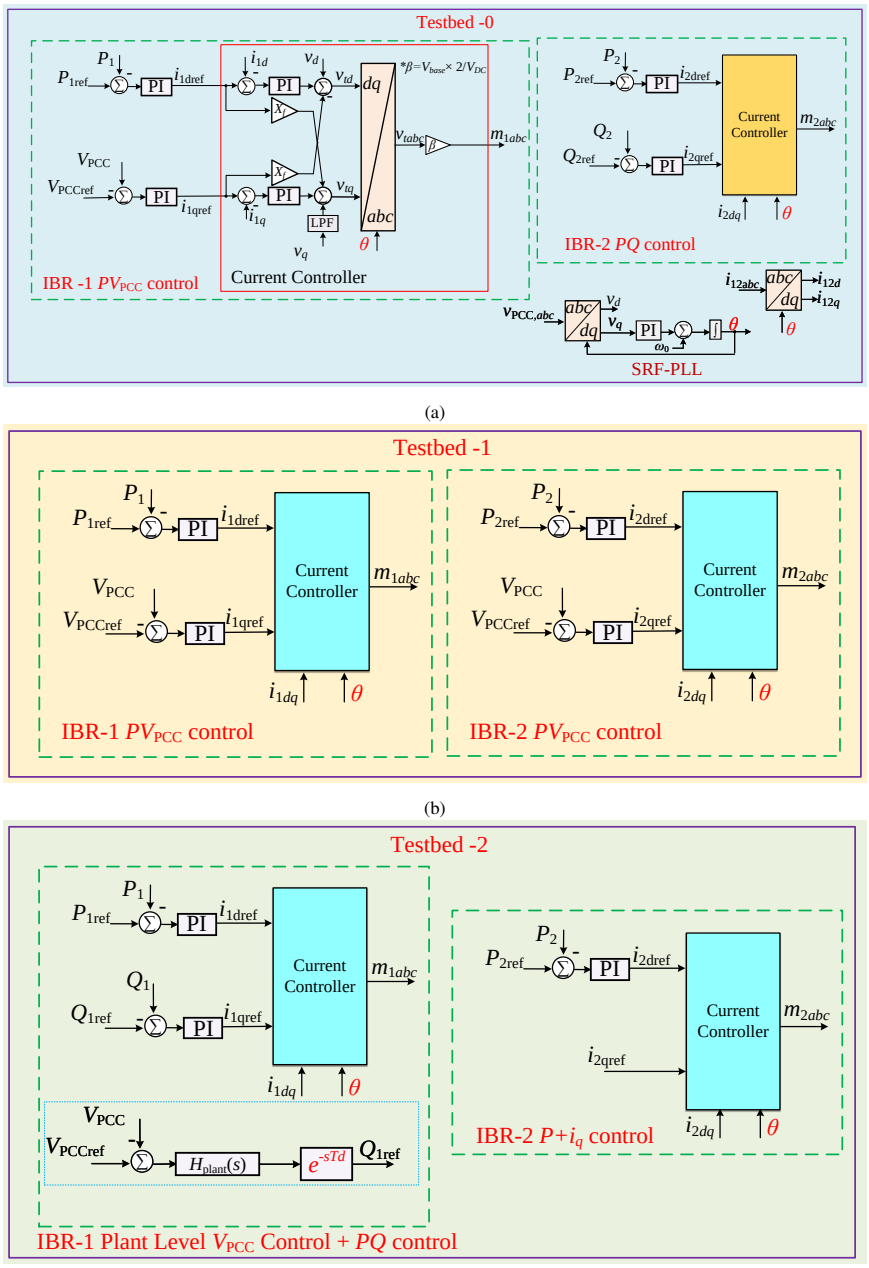

Fig. 2: Control structures for Testbed-0, Testbed-1, and Testbed-2.

Both the IBRs are grid-following inverters. The subscripts "1" and "2" represent IBR-1 and IBR-2 respectively. In this paper, three testbeds with different control structures are considered for the study.

A. Testbed-1

In Testbed-1, the two IBRs have identical controls. The inner current control is implemented in the PLL-based dq frame, and the outer control regulates real power P and the PCC bus voltage V_{PCC}. The real power control generates $i_{d\text{ref}}$ for the d-axis current control and the voltage control generates $i_{q\text{ref}}$ for the q-axis current control. A synchronous reference frame-PLL is used to synchronize the PCC voltage to the grid. The output angle (θ) from the PLL is used for frame conversion. The real power P_1 and the reactive power Q_1 are given by:

$$\begin{aligned} P_1 &= v_d\, i_{1d} + v_q\, i_{1q} \\ Q_1 &= v_q\, i_{1d} - v_d\, i_{1q} \end{aligned} \tag{1}$$

Here, v_d and v_q are the dq components of v_{PCC}. Similarly, P_2 and Q_2 are defined. The magnitude of the PCC bus voltage is obtained as:

$$V_{\text{PCC}} = \sqrt{v_d^2 + v_q^2} \tag{2}$$

Additionally, a feed-forward filter (VFF) has been added to the feed-forward signal v_q in the inner current control to enhance the system stability. The feed-forward filter is a low pass filter and the transfer function is $\frac{1}{T_{vf}\, s+1}$, where T_{vf} is the cutoff frequency.

TABLE I: Parameters of Testbeds.

Description	Parameter	Value
Power Base	S_b	100 MVA
Voltage Base	V_b	575 V
Nominal Frequency	f_0	60 Hz
Grid Voltage	V_g	575 V
DC Voltage	V_{DC}	1100 V
Choke Filter	X_f	0.15 pu
	R_f	0.003 pu
	B_c	0.1 pu
Transmission Line Inductance	X_g	1 pu
Transmission Line Resistor	R_g	$0.1X_g$ pu
Control Parameters for Testbed 1		
Inner Loop Control	k_{ip}, k_{ii}	0.3, 5
Outer Loop Control,P control	k_{Pp}, k_{Pi}	0.4, 40
Outer Loop Control,V_{PCC}	k_{Vp}, k_{Vi}	0.4, 40
Feed-forward filter	T_{vf}	0.002
Control Parameters for Testbed-2		
Inner Loop Control	k_{ip}, k_{ii}	0.3, 5
Outer Loop Control,P control	k_{Pp}, k_{Pi}	0.4, 40
Outer Loop Control, Q/V_{PCC} control	k_{Vp}, k_{Vi}	0.4, 40
Feed-forward filter	T_{vf}	0.001
Plant Level Control	$k_{i\text{Plant}}$	10
Plant Level delay	T_d	5 ms
PLL	$k_{\text{PLL}p}$, $k_{\text{PLL}i}$	60, 1400
Control Parameters Grid Forming IBR		
Inner Loop Control	k_{ip}, k_{ii}	0.3, 5
Outer Loop Control	k_{Vp}, k_{Vi}	2, 10
P–f droop	n_p	0.2

B. Testbed-2

For Testbed-2, IBR-1 and IBR-2 have different control structures for the outer control. The inner current controls are the same. For IBR-1, the d-axis outer control is the real power control, whereas in the q-axis control, the outer control is reactive power control. The reactive power order is generated from the plant-level voltage controller. For the plant-level control, the voltage reference order ($V_{\text{PCC,ref}}$) is compared with the measurement V_{PCC} and passed through an integral controller ($\frac{k_{i\text{Plant}}}{s}$) to generate the reactive power order ($Q_{1,\text{ref}}$). Additionally, a delay ($e^{-T_d s}$) is considered for the plant-level control and inverter-level control communication. IBR-2 shares the same d-axis outer loop control structure as IBR-1 but does not have q-axis outer loop control and $i_{2,q\text{ref}}$* = 0.

C. Testbed-0

Testbed-0 is used to compare with Testbed-1 and show the necessity of coordination. In Testbed-0, IBR-1 and IBR-2 have different outer loop control, but the inner current control is the same. For IBR-1, the outer loop is real power P and PCC bus voltage V_{PCC} control, whereas IBR-2 has an outer loop in real power P and reactive power Q control. The rest of the control structure is similar to Testbed-1.

The detailed controller structures of Testbed-0, Testbed-1, and Testbed-2 are presented in Fig. 2. The parameters for Testbed-0, Testbed-1, and Testbed-2 are presented in Table I. The controller gains are based on the per-unit system.

III. Coordination Philosophy and Analysis

In this section, the coordination philosophy is explained using a two-IBR system presented in Fig. 3, with each IBR represented as a controllable current source.

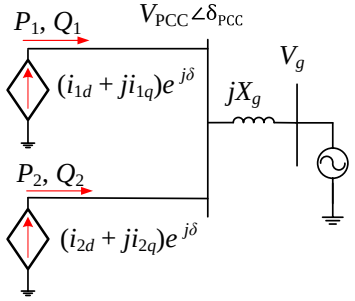

Fig. 3: Simple representation of a two-IBR system.

The transmission line's resistance and electromagnetic dynamics are neglected. Hence, jX_g is used to represent the transmission line. The two IBRs adopt vector control [19], [20] in the dq frame, where the d axis of the frame is aligned with PCC bus voltage's space vector. This simplified model is adapted from the senior authors' prior work [15]. In [15], the author has developed a linear feedback system to explain weak grid stability. It is found that the PCC bus voltage magnitude is directly related to the PLL angle δ (where $\delta = \Delta\theta = \theta - \omega_0 t$, and ω_0 is the nominal angular frequency). The d-axis outer control exerts influence on the PCC bus phase angle through the d-axis current.

In the following, a feedback system for a two-IBR system is derived. Based on the circuit shown in Fig. 3, the following relationship is obtained:

$$V_{\text{PCC}}e^{j\delta_{\text{PCC}}} = jX_g(i_{1d} + ji_{1q} + i_{2d} + ji_{2q})e^{j\delta} + V_g \quad (3)$$

Here, δ_{PCC} is the PCC bus angle, δ is the angle from the PLL. Linearizing right-hand side (RHS) and left-hand side (LHS) (3) we get:

$$\begin{aligned}\text{LHS} &= e^{j\delta_{\text{PCC}}}\Delta V_{\text{PCC}} + jV_{\text{PCC}}e^{j\delta_{\text{PCC}}}\Delta\delta_{\text{PCC}} \\ \text{RHS} &= X_g e^{j\delta}[j(\Delta i_{1d} + \Delta i_{2d}) \\ &\quad - \Delta i_{1q} - \Delta i_{2q} - \Delta\delta(i_{1d} + i_{2d} + ji_{1q} + ji_{2q})]\end{aligned} \quad (4)$$

At steady state $\delta_{\text{PCC}} = \delta$, and comparing real and imaginary parts of RHS and LHS, we get:

$$\begin{aligned}\Delta V_{\text{PCC}} &= -X_g(i_{1d} + i_{2d})\Delta\delta - X_g(\Delta i_{1q} + \Delta i_{2q}) \\ \Delta\delta_{\text{PCC}} &= \frac{X_g}{V_{\text{PCC}}}\left(\Delta i_{1d} + \Delta i_{2d} - (i_{1q} + i_{2q})\Delta\delta\right)\end{aligned} \quad (5)$$

In (5), assuming $i_{1q} + i_{2q} = 0$, and $G_{\text{PLL}}(s)$ is the transfer function from $\Delta\delta_{\text{PCC}}$ to $\Delta\delta$, and re-arranging (5) we arrive at:

$$\begin{aligned}\Delta V_{\text{PCC}} = &\underbrace{-X_g(i_{1d} + i_{2d})\frac{X_g}{V_{\text{PCC}}}}_{c} G_{\text{PLL}}(s)(\Delta i_{1d} + \Delta i_{2d}) \\ &- X_g(\Delta i_{1q} + \Delta i_{2q})\end{aligned} \quad (6)$$

From (6), we can conclude that for a two IBR system, ΔV_{PCC} has contributions from Δi_{1d}, Δi_{2d}, Δi_{1q}, and Δi_{2q}. In this paper, PLL is designed to have a bandwidth of 13 Hz, as per the parameters of the PI gains as 60 and 1400. The Bode diagram is presented in Fig. 4. For our study, the concerned frequency range is less than 10 Hz. Hence, we can

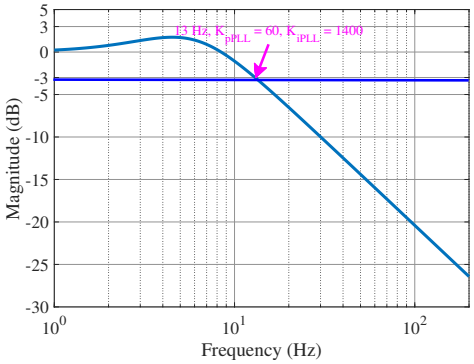

Fig. 4: Bode diagram of the 13-Hz PLL's transfer function G_{PLL}.

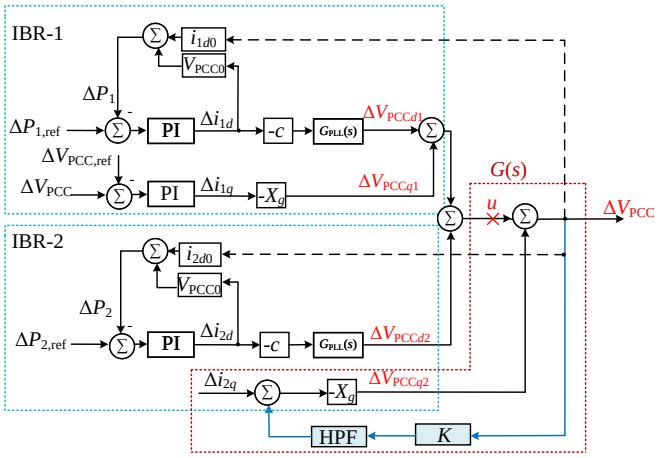

Fig. 5: Block diagram with the stability enhancement strategy for a two-IBR system.

safely assume in this frequency range, PLL does not interfere with the dynamics of the system, i.e., $G_{\mathrm{PLL}}(s)$ =1.

A linear relationship is also found for the real power and the reactive power for both IBRs.

$$\begin{aligned}\Delta P_1 &= i_{1d0}\Delta V_{\mathrm{PCC}} + V_{\mathrm{PCC}}\Delta i_{1d}\\ \Delta Q_1 &= -i_{1q0}\Delta V_{\mathrm{PCC}} - V_{\mathrm{PCC}}\Delta i_{1q}\end{aligned} \tag{7}$$

Similarly, expressions for ΔP_2 and ΔQ_2 are obtained. With the help of (6) and (7), a linear block system of the two-IBR system is constructed as shown in Fig. 5.

A. Weak Grid Voltage Instability: The Critical Reason

The block diagram clearly shows the coupling between the real power control and the PCC voltage. At weak grid conditions, X_g is large. Thus, a weak grid and high power transfer may lead to a large value of c. According to (6) and the block diagram, an increase in the power order will result in the increase in Δi_d and in turn the reduction of ΔV_{PCC}. This may cause ΔP to reduce. Hence, if the effect of Δi_d on voltage is overwhelming, ΔP may not follow the power order, introducing an instability mechanism. More details on the instability mechanism can be found in [21] and [22]. Since the instability is mainly due to the high sensitivity of voltage towards current injection in weak grids, this type of instability is termed as voltage stability.

B. Importance of Coordination

It has been now known that inverters with fast voltage control can achieve better stability [17], [23] by making the inverter behave like a voltage source. Therefore, voltage control is usually assumed in the literature to achieve better stability, e.g., [16], [17]. On the other hand, in a two-IBR system, IBRs having identical control, (either power and voltage–PV or power and reactive power–PQ control) vs. IBRs having different control modes do not necessarily work better. We have found that with one IBR in PV control and another in PQ control mode, the entire system can achieve better stability.

The comparison results are presented as follows for a step change in the power order. Testbed-0 has IBR-1 in the PV control mode and IBR-2 in the PQ control mode, while Testbed-1 has both IBR working under the PV control mode. The control structure has been presented in Fig. 2. The results are presented in Fig. 6. Under similar weak grid conditions (SCR $\approx$ 1), Testbed-0 shows better stability, while Testbed-1 goes to an unstable condition.

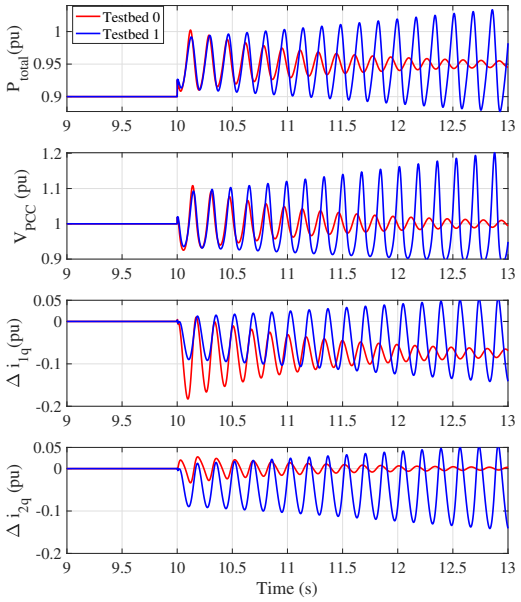

Fig. 6: Time-domain simulation results for total real power (P_{total}), PCC voltage, and the q-axis current deviations. Testbed-0 and Testbed-1 are under very weak grid conditions (X_g =1 pu). The Q controller PI gains for IBR-2 in Testbed-0 are (2,25), whereas, in Testbed-1, the V controller PI gains for IBR-2 is (0.25,25).

Hence, it is found that how the q-axis current is controlled matters. Proper coordination of the reactive current control among inverters can help improve stability. This motivates a detailed examination on the relationship between voltage and the q-axis current, as elaborated below.

C. Philosophy of Coordination and Control Enhancement

The key philosophy of coordination of IBR is developed after examining AEMO's success in identifying the source of 7-Hz oscillations in west Murray [24], [25]. Five solar farms were pinpointed as the negative influencers. The critical

technology in identifying the five troublemakers is essentially observing the phase shift between voltage (V) and reactive power (Q) output from each IBR under 7-Hz perturbation. If V and Q are in phase, this IBR contributes to the oscillation mode. On the other hand, if V and Q are out of phase, this IBR is mitigating the oscillation (other IBRs cause the oscillation).

From the physics point of view, in the low-frequency range (ignoring very fast transmission line electromagnetic dynamics), it is well known that injecting reactive power into a grid can cause an increase in voltage. The mathematical relationship is as follows:

$$\Delta V \approx X_g \Delta Q \approx -X_g \Delta i_q, \tag{8}$$

where X_g is the grid reactance. Note that the above simplified relationship has ignored the effect of real power and/or real current i_d's effect on voltage. A relationship between ΔV and dq current has been presented in (6).

This relationship is based on the well-known relationship between the reactive power injection and voltage. Reference [26] has used the same insight to explaining the wind turbine var oscillations. Also in [27], a similar expression has been used to explain oscillations in parallel a solar PV and a battery energy storage system.

If there are two IBRs connected to the point of interconnection, the voltage will have contributions from the reactive current injection from both IBRs. The equation can be modified as:

$$\Delta V \approx \underbrace{-X_g \Delta i_{1q}}_{\Delta V_1} + \underbrace{-X_g \Delta i_{2q}}_{\Delta V_2} \tag{9}$$

It is possible that ΔV_1 and ΔV are in phase while ΔV_2 and ΔV are out of phase, which implies that IBR-1 contributes to oscillations and is the negative influencer while IBR-2 mitigates oscillations and is the positive influencer.

Consequently, the above remarks explain the comparison results in Fig. 6. It can be seen that in Testbed-1 when both IBRs are in the voltage control mode, both reactive powers (currents) contribute to the oscillations. On the other hand, when IBR-2 changes its control mode, IBR-2's reactive power or reactive current contributes less to the oscillation.

Therefore, we have one more means to push the limit besides carefully designing/improving individual IBR controls. We can coordinate IBR controls to make further improvements.

Our philosophy is to have one or more IBRs provide damping through counter reactive power. To achieve this goal, an IBR has to be designed to have its q-axis current order modulated by the positive feedback of voltage deviation. For the two-IBR system, IBR-2's q-axis current order will be modulated.

$$\Delta i_{q2} \approx \Delta i^*_{q2} = k\Delta V, \Longrightarrow \Delta Q_2 \approx -V\Delta i_{q2} \propto -\Delta V \tag{10}$$

Based on (7), $\Delta Q_2 = -V\Delta i_{q2} - i_{2q0}\Delta V$. Assuming that the initial q-axis current is 0 or IBR-2 is not providing nor absorbing significant reactive power, $\Delta Q_2 \approx -V\Delta i_{q2}$. Hence, when the q-axis current order is modulated to be proportional to ΔV, the resulting reactive power modulation ΔQ_2 counters ΔV and can mitigate voltage oscillations.

D. Control Implementation

The control strategy includes modulating one group of IBR's q-axis current order according to the voltage deviation. This is achieved by the feedback of PCC voltage signal V_{PCC} after passing through a high-pass filter (HPF) with a transfer function $\frac{\tau s}{\tau s+1}$. Here, $1/\tau$ is the cutoff frequency of the HPF filter. An additional gain K is added to provide flexibility. The control is implemented in the multi-IBR system linear block diagram as shown in Fig. 5.

The transfer function from u (aggregated effect of Δi_{1d}, Δi_{1q} and Δi_{2d} on the PCC voltage) to ΔV_{PCC} is given by:

$$\begin{aligned} G(s) &= \frac{1}{1 + X_g \text{HPF}} = \frac{1}{1 + X_g\, K\, \frac{\tau s}{1+\tau s}} \\ &= \frac{1+\tau s}{1 + s\tau(X_g K + 1)} \end{aligned} \tag{11}$$

Without the feedback, $G_s = 1$. From (11), we can conclude the transfer function imitates a low-pass filter (LPF). The Bode diagrams of the transfer function for $X_g = 1.0$, $\tau = 0.1$ s and for different parameters of K are presented in Fig. 7. From Fig. 7, it is observed that the cutoff frequency for $K = 1$, is around 1.1 Hz. It can be seen that for 6-Hz oscillations, the HPF-based control can effectively reduce the loop gain to 18% of the original gain when K is 5, thereby significantly increasing the oscillation stability margin.

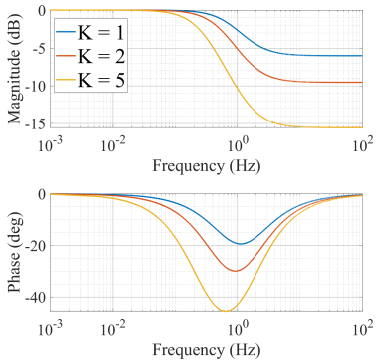

Fig. 7: Bode diagram of the transfer function $G(s)$ which imitates the behavior of a LPF. $X_g = 1.0$ p.u. and $\tau = 0.1$ s.

Remarks: The gain of the transfer function $G(s)$ is unity without the HPF controller. With the feedback controller, the gain of the transfer function is reduced in the region of several Hz for more than 5 dB. Hence, the coupling between the dq-axis current and the ΔV_{PCC} is also decreased. Thus, the HPF controller is beneficial for weak grid voltage stability.

E. Linear Model-Based Analysis

The block diagram presented in Fig. 5 is built in MATLAB/Simulink. The following operating condition is assumed: $P_{1,\text{ref}} = P_{2,\text{ref}} = 0.5$ p.u. , and V_{PCC} is maintained at 1 p.u. A small step change of 1% is applied in $\Delta P_{1,\text{ref}}$. The simulation results in Fig. 8 show that the system undergoes poorly damped oscillations of about 7 Hz. When the HPF control is enabled, the oscillations are damped out. The selected parameters for the stability controller are $\tau = 0.1$ s and $K = 5$.

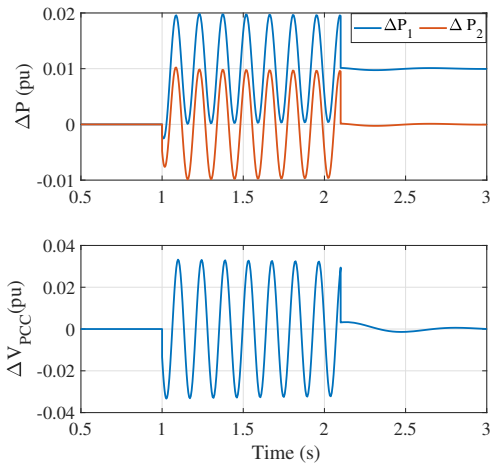

Fig. 8: Time-domain results to demonstrate the effects of stability controller in mitigation of weak grid oscillations. When the controller is disabled 7 Hz oscillations are observed when a step change is introduced $\Delta P_{1,\text{ref}}$ of 0.01 pu at $t = 1$ s. The HPF controller is enabled at $t = 2.1$ s and the oscillations are mitigated.

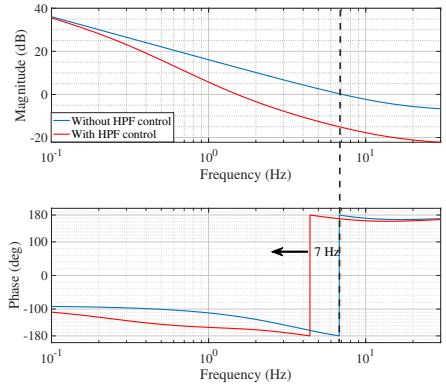

Fig. 9: Bode diagram of open-loop system from u to u. Blue curve presents the open-loop transfer function without the HPF controller and at 7 Hz system is marginally stable. The red curve presents the transfer function with the HPF controller which indicates a stable system at 7 Hz.

Further investigation is conducted in the frequency domain by analyzing the open-loop transfer function. The open-loop system is obtained by breaking at the point marked a red cross in Fig. 5. The transfer function obtained is from u to ΔV_{PCC}. The Bode diagram is presented in Fig. 9. It is observed that without the HPF controller, the phase shifting occurs at 7 Hz and the gain margin at this point is 0 dB, which implies a marginally stable system. After the addition of the HPF controller (red curve), the system is stable at the 7 Hz frequency point with a positive gain margin. This observation is in coherence with the time-domain results presented in Fig. 8. It can be seen that the HPF controller makes $G(s)$ (from u to ΔV_{PCC}) act as a LPF and effectively reduce the open-loop gain in the several Hz region. In turn, it enhances stability.

IV. Electromagnetic Transient (EMT) Simulations

The three testbeds presented in Section II are simulated in MATLAB/Simscape Electrical. EMT simulations are conducted with the SCR at 1.0 p.u. The HPF-based voltage feedback is introduced in IBR-2 for all three testbeds to modulate its q-axis current order, as shown in Fig. 10. Two tests (small disturbance and large disturbance) are conducted for each testbed to demonstrate the advantage of HPF control. The IBRs in the three testbeds are all adopting grid-following control (GFL). Furthermore, the HPF control is also tested for grid-forming control (GFM). The parameters in Table I are used for IBR controls.

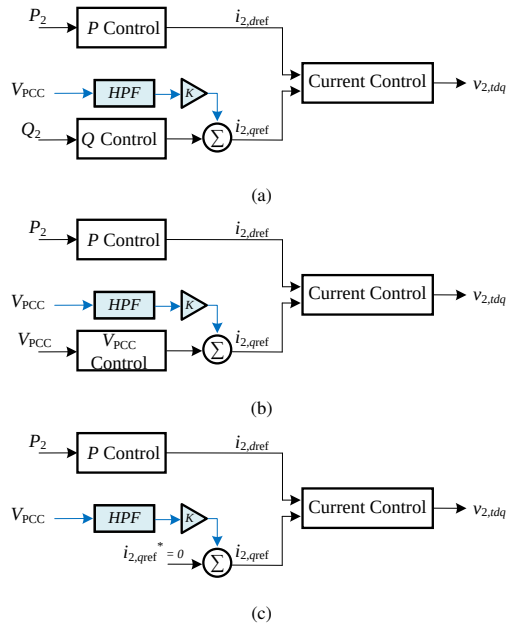

Fig. 10: IBR-2 with the voltage feedback control. (a) Testbed-0; (b) Testbed-1; (c) Testbed-2.

A. Small Disturbance Tests: Power Order Increase

For the first test, the power order of the two IBRs is increased in steps. For Testbed-0, when IBR-1 is at 0.44 pu, and IBR-2 at 0.5 pu, the system undergoes poorly damped oscillations of about 6 Hz. For Testbed-1, when the power orders of IBR-1 and IBR-2 are 0.474 p.u. and 0.5 p.u. (i.e., total power output is 0.974 p.u.) respectively, the system experiences low-frequency oscillations. The frequency of the oscillations is 6.5 Hz. A similar power order increase is implemented in Testbed-2. When $P_{1,\text{ref}} = 0.55$ p.u. and $P_{2,\text{ref}} = 0.3$ p.u., the system undergoes 3.2-Hz oscillations.

Selection of HPF parameters: The HPF feedback control is implemented in IBR-2. The parameters for the feedback control are the HPF's time constant τ and the gain K. The selected values for Testbed-1, and Testbed-2 are listed in Table. II. In Testbed-0, the oscillation frequency is 6 Hz, and HPF parameters of 0.5 s and 3 provide sufficient damping to mitigate the 6 Hz oscillations. For Testbed-1, the oscillation frequency is about 6.5 Hz, hence the time constant at 0.1 s and the gain at 5 can provide a sufficient gain reduction in the frequency region. On the other hand, Testbed-2 has an oscillation frequency of 3.2 Hz. Though the same control can provide gain reduction at 3.2 Hz, it also introduces a phase lag of more than 20°. To have a smaller phase lag, the time constant 0.2 s and the gain 1 are used for Testbed-2.

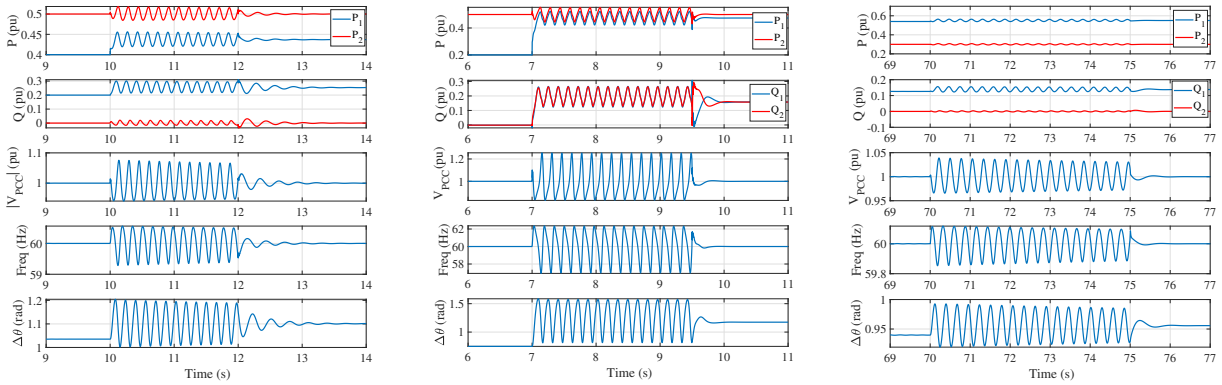

Fig. 11: Small disturbance tests: time-domain response of P, Q, V_{PCC}, f_{PLL} and $\Delta\theta$. The figure presents the system's response with and without the introduction of HPF stability controller when subject to real power order increase. (a) Testbed-0: HPF controller is enabled at t = 12 s. The controller mitigates 6 Hz oscillations. (b) Testbed-1: The HPF voltage control is enabled at $t = 9.5$ s. The controller mitigates the 6.5-Hz weak grid oscillations. (c) Testbed-2: The HPF voltage control is enabled at $t = 75$ s. The controller mitigates 3.2-Hz oscillations.

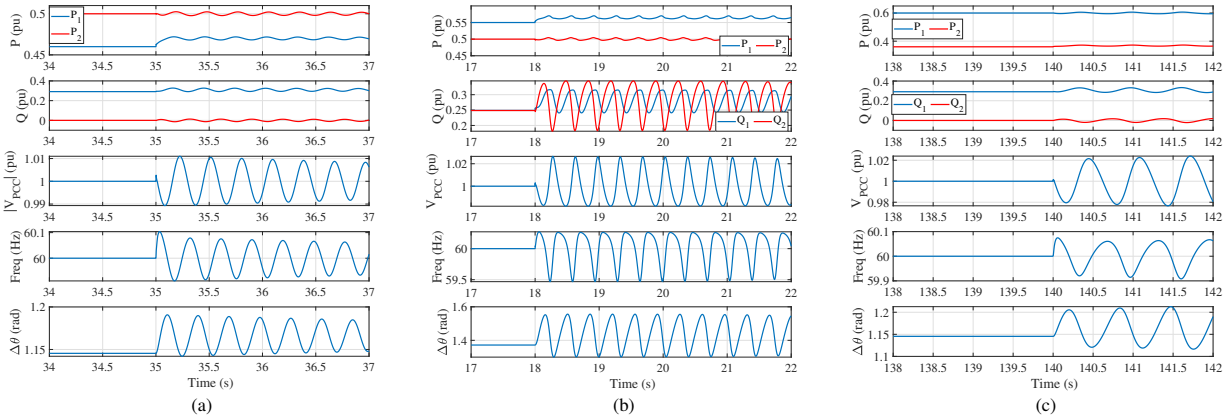

Fig. 12: Small disturbance tests: time-domain responses of real power P, reactive power Q, V_{PCC}, frequency and PLL angle $\Delta\theta$. The results indicate that the power transfer capability increased after the stability controller's introduction. (a) Testbed-0 is able to push around 0.96 p.u..(b) Testbed-1 is able to push 1.06 p.u. power where, as (c) Testbed-2 can push around 0.97 p.u. power.

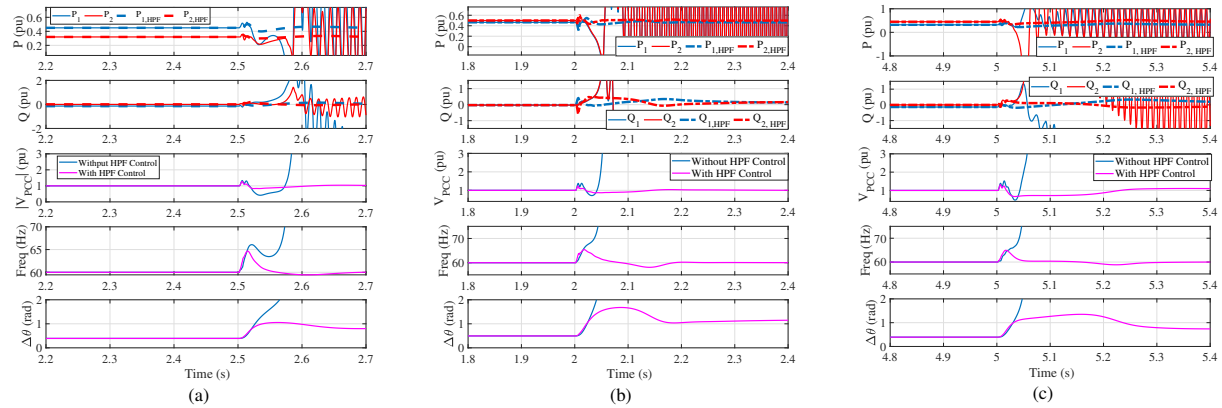

Fig. 13: Large disturbance (line tripping) tests. P, Q, V_{PCC}, f_{PLL} and $\Delta\theta$ when X_g changes from 0.5 p.u. to 1 p.u. (a) Testbed-0; (b) Testbed-1; (c) Testbed-2.

TABLE II: Feedback control parameters selected for Testbed-1 and Testbed-2.

	τ	K	power transfer increase
Testbed-0	0.5	3	3.5%
Testbed-1	0.1	5	9%
Testbed-2	0.2	1	14%

Enabling the feedback control in IBR-2 mitigates the 6-Hz oscillations in Testbed-0, the 6.5-Hz oscillations in Testbed-1, and 3.2-Hz oscillations in Testbed-2. The dynamic responses of the real power P, reactive power Q, PCC bus voltage V_{PCC}, and the output from the PLL (frequency, and the angle $\Delta\theta$) for IBRs are presented in Fig. 11. It can be clearly seen that the HPF control mitigates the weak grid oscillations in all the

cases.

For Testbed-0, with the added controller, the power exporting capability of the two IBRs increases from 0.937 p.u. to 0.97 pu, a 3.5% increase. For Testbed-1, with the added controller, the power exporting capability of the two IBRs increases from 0.974 p.u. to 1.064 pu, a 9% increase. While for Testbed-2, the power transfer capability increases from 0.85 p.u. to 0.97 p.u. i.e., 14% increase. For Testbed-1, the power transfer is close to the steady-state limit (1.1 p.u.) associated with X_g = 1 p.u. The simulation results at the marginal stable conditions are presented in Fig. 12.

Remarks:

1) The HPF controller is able to mitigate weak grid oscillations (6.5 Hz and 3.2 Hz) for different scenarios. This capability shows the robustness of the control.
2) The HPF control helps increase the stability margin of multi-IBR systems.
3) The HPF control does not change steady-state operating conditions.

B. Large Disturbance Tests: Line Tripping

Furthermore, large disturbance tests are conducted to emulate a transmission line tripping event. For both testbeds, X_g changes from 0.5 (SCR $\approx$ 2) to X_g = 1.0 (SCR $\approx$ 1). Without the feedback control strategy, the system loses its synchronism and becomes unstable. With feedback control, the system remains stable and sustains the large disturbance.

The results for the line tripping event are presented in Fig. 13. For Testbed-0, the line trip event happens at $t = 2.5$ s, and the total power output is 0.77 pu (P_1 = 0.45 p.u., and P_2 = 0.32 p.u.). For Testbed-1, at $t = 2s$, X_g changes from 0.5 p.u. to 1.0 p.u. The total power output from both IBRs is 0.95 pu (P_1 = 0.45 pu, and P_2 = 0.5 pu). While for Testbed-2, the line trip event happens at $t = 5$ s, and the total power output is 0.77 pu (P_1 = 0.45 p.u., and P_2 = 0.32 p.u.).

C. Grid Forming Converter

Further investigation is done on the effectiveness of a stability enhancement strategy for a single grid-forming inverter operating under weak grid conditions. Our prior research shows that under weak grid conditions, oscillations may appear [28], [29]. The system topology and control structure used in the study is depicted in Fig. 14, with the control structure being adapted from the works of [30], [31]. Detailed parameters are provided in Table. I. Under weak grid conditions, when the reference power output, P_{ref}, was set to 0.92, the system exhibited poorly damped oscillations with a frequency of approximately 4 Hz. We enable the HPF controller, which effectively mitigated the oscillations. Consequently, the system could now sustain a power output of around 1.04 per unit (pu) before encountering instability. The results are presented in Fig. 15.

V. Hardware Validation

To further substantiate the proposed stability feedback control scheme, a laboratory-scale hardware testbed is established.

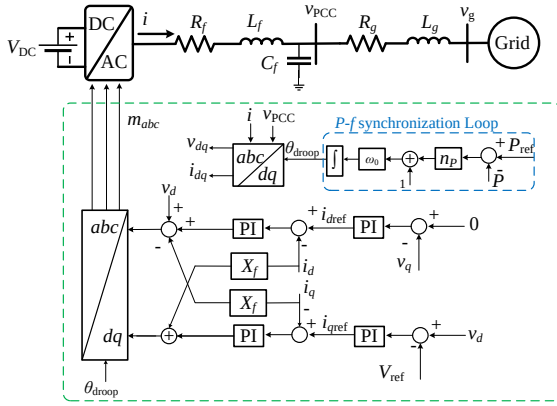

Fig. 14: System topology of grid-connected grid forming converter.

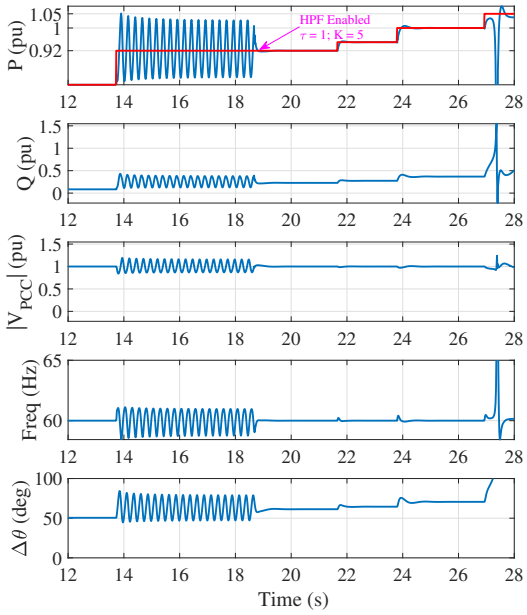

Fig. 15: Time-domain responses of real power P, reactive power Q, V_{PCC}, frequency and PLL angle $\Delta\theta$. The results indicate that the power transfer capability increased after the stability controller's introduction.

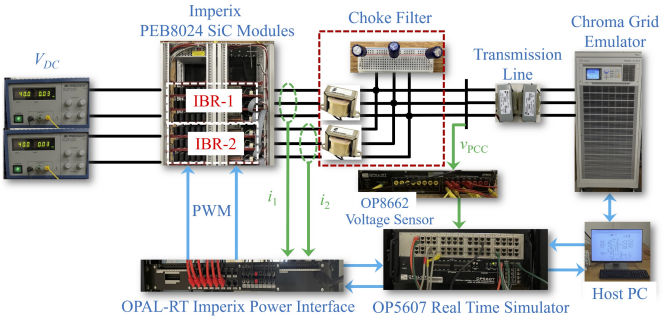

Fig. 16: Laboratory scale hardware testbed for experimental validation.

The hardware testbed includes two three-phase converters consisting of 6 Imperix PEB8024 half-bridge power modules, Chroma Regenerative Grid Simulator 61845 acting as power grid source, Opal RT's OP5607 real-time simulator for control algorithm implementation, analog voltage and current sensors, DC power supply and other passive elements. The detailed

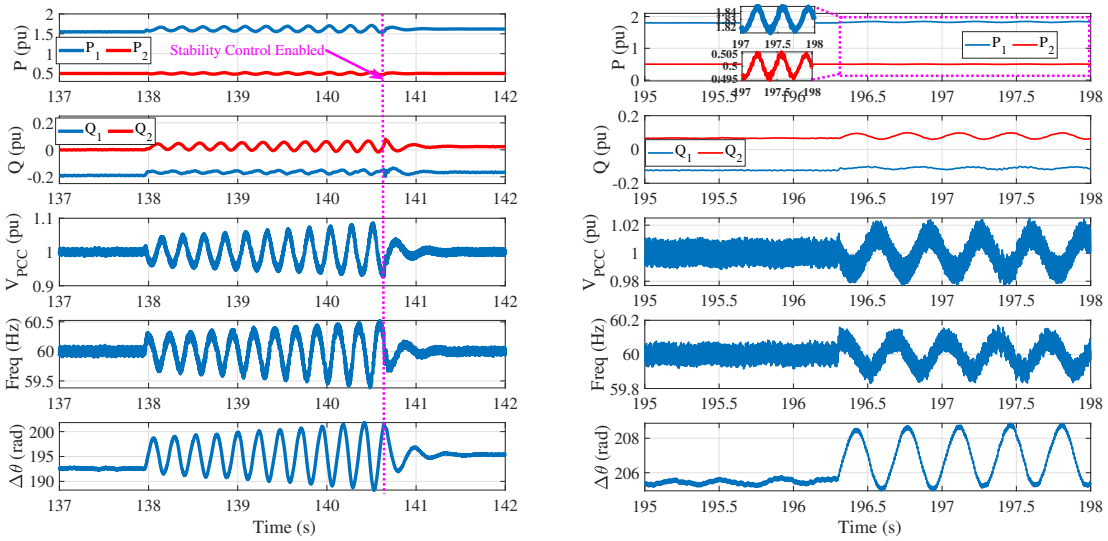

Fig. 17: Hardware experiment results. (a) Time domain responses when the power order is increased. The results show the performance of the stability controller in mitigating the 4 Hz oscillations. (b) The results show the stability controller's performance in terms of increased power transfer capability of the system. The steady-state power transfer limit for the hardware test bed is 2.58 p.u.

structure of the hardware testbed is presented in Fig. 16. The control algorithm is implemented using MATLAB-based RT-Lab on the host PC. Similarly, the Chroma Grid emulator is also controlled remotely using LabVIEW.

Both the inverters are in real power and PCC voltage regulation mode. The system strength as observed by the two IBRs at the PCC bus is 2.18 (X_g = 0.457 p.u.). The steady-state power limit corresponding to X_g = 0.457 p.u. and R_g = 0.0950 p.u. is 2.578 p.u. The testbed parameters are tabulated in Table III.

The power order is increased in small steps for IBR-1, while the power order for IBR-2 is kept at $P_{2,\text{ref}}$ = 0.5 p.u. Initially, the stability control is disabled. When the power output from IBR-1 is 1.62 p.u the system undergoes poorly damped 4-Hz oscillations. After the occurrence of the oscillations, the HPF stability control is enabled at $t = 141.5$ s, which mitigates the oscillations. The results are shown in Fig. 17(a). The parameters selected for the HPF stability control are $K = 2$, and $\tau = 0.1$ s.

Furthermore, with the stability control enabled, the system is marginally stable when IBR-1 power output level is 1.83 p.u. while the IBR-2 is still exporting 0.5 p.u., as shown in Fig. 17(b). The experimental validation demonstrates the efficacy of the proposed stability controller.

Remarks: With the stability control, the total power output increased from 2.05 p.u. to 2.3 p.u., about 12% increase. The steady-state limit is 2.578 p.u.

VI. Conclusions

By employing a suitable coordination scheme, a multi-IBR system has increased stability margin while operating in very weak grid conditions. Furthermore, with one group of IBR's q-axis current orders modulated by a voltage feedback, the effect is similar as reducing the coupling between the VSC's real power control and the PCC voltage. This effect helps enhance weak grid voltage stability. The coordination can be implemented by feedbacking of the PCC bus voltage after passing it through a high-pass filter. Linear analysis, EMT-based computer simulation, and hardware experiments all confirm the efficacy of the stability enhancement strategy. In addition, the strategy is simple and straightforward for implementation and is robust against the host system. Variety of control structures, including GFL and GFM, have been tested. Therefore, it leads to high practical values.

TABLE III: Parameters used for experimental validation.

Description	Parameter	Value
Power Base	S_b	50 VA
Voltage Base	V_b	20 V
Nominal Frequency	f_0	60 Hz
Grid Voltage	V_g	20 V
DC Voltage	V_{DC}	40 V
Choke Filter	X_f	0.0707 pu
	R_f	0.0034 pu
	B_c	0.1417 pu
Transmission Line Inductance	X_g	0.457 pu
Transmission Line Resistor	R_g	0.0950 pu
Inner Loop Control	k_{ip}, k_{ii}	1, 10
Outer Loop Control,P control	k_{Pp}, k_{Pi}	0.25, 25
Outer Loop Control,V_{PCC}	k_{Vp}, k_{Vi}	0.25, 25
Feed-forward filter	T_{vf}	0.002
PLL	$k_{\text{PLL}p}$, $k_{\text{PLL}i}$	60, 1400
Switching Frequency	f_{SW}	5 kHz

References

[1] H. Holttinen, A. Groom, E. Kennedy, D. Woodfin, L. Barroso, A. Orths, K. Ogimoto, C. Wang, R. Moreno, K. Parks, and T. Ackermann, "Variable renewable energy integration: Status around the world," *IEEE Power and Energy Magazine*, vol. 19, no. 6, pp. 86–96, Nov 2021.

[2] B. Badrzadeh, Z. Emin, S. Goyal, S. Grogan, A. Haddadi, A. Halley, A. Louis, T. Lund, J. Matevosyan, T. Morton, D. Premm, and S. Sproul, "System strength," *CIGRE Science and Technology Journal:*, vol. 21, Feburary 2021.

[3] S.-H. Huang, J. Schmall, J. Conto, J. Adams, Y. Zhang, and C. Carter, "Voltage control challenges on weak grids with high penetration of wind generation: ERCOT experience," in *2012 IEEE Power and Energy Society General Meeting*. IEEE, 2012, pp. 1–7.

[4] C. Li, "Unstable operation of photovoltaic inverter from field experiences," *IEEE Transactions on Power Delivery*, vol. 33, no. 2, pp. 1013–1015, 2018.

[5] A. Jalali, B. Badrzadeh, J. Lu, N. Modi, and M. Gordon, "System strength challenges and solutions developed for a remote area of Australian power system with high penetration of inverter-based resources," *CIGRE Sci. Eng. J.*, pp. 27–37, 2021.

[6] Y. Cheng, L. Fan, J. Rose, F. Huang, J. Schmall, X. Wang, X. Xie, J. Shair, J. Ramamurthy, N. Modi, C. Li, C. Wang, S. Shah, B. C. Pal, Z. Miao, A. Isaacs, J. Mahseredjian, and Z. J. Zhou, "Real-world subsynchronous oscillation events in power grids with high penetrations of inverter-based resources," *IEEE Transactions on Power Systems*, pp. 1–1, 2022.

[7] L. Fan, Z. Miao, S. Shah, Y. Cheng, J. Rose, S.-H. Huang, B. Pal, X. Xie, N. Modi, S. Wang, and S. Zhu, "Real-world 20-hz IBR subsynchronous oscillations: Signatures and mechanism analysis," *IEEE Transactions on Energy Conversion*, vol. 38, no. 1, pp. 316-330, Jan. 2023.

[8] B. Wen, D. Boroyevich, R. Burgos, P. Mattavelli, and Z. Shen, "Analysis of d-q small-signal impedance of grid-tied inverters," *IEEE Transactions on Power Electronics*, vol. 31, no. 1, pp. 675–687, 2016.

[9] NERC, "Integrating InverterBased Resources into Low Short Circuit Strength Systems," North American Electric Reliability Corporation, Tech. Rep., 12 2017.

[10] L. Huang, C. Wu, D. Zhou, and F. Blaabjerg, "A double-PLLs-based impedance reshaping method for extending stability range of grid-following inverter under weak grid," *IEEE Transactions on Power Electronics*, vol. 37, no. 4, pp. 4091–4104, 2022.

[11] S. Almutairi, Z. Miao, and L. Fan, "Stability analysis of two types of g rid-forming converters for weak grids," *International Transactions on Electrical Energy Systems*, vol. 31, no. 12, p. e13136, 2021.

[12] C. Guo, W. Liu, C. Zhao, and R. Iravani, "A frequency-based synchronization approach for the VSC-HVDC station connected to a weak ac grid," *IEEE Transactions on Power Delivery*, vol. 32, no. 3, pp. 1460–1470, 2017.

[13] C. Li, S. Wang, F. Colas, and J. Liang, "Dominant instability mechanism of vsi connecting to a very weak grid," *IEEE Transactions on Power Systems*, vol. 37, no. 1, pp. 828–831, 2022.

[14] H. Gong, X. Wang, and L. Harnefors, "Rethinking current controller design for PLL-synchronized VSCs in weak grids," *IEEE Transactions on Power Electronics*, vol. 37, no. 2, pp. 1369–1381, 2022.

[15] L. Fan, "Modeling type-4 wind in weak grids," *IEEE trans. Sustainable Energy*, vol. 10, no. 2, pp. 853–864, 2019.

[16] A. Egea-Alvarez, S. Fekriasl, F. Hassan, and O. Gomis-Bellmunt, "Advanced vector control for voltage source converters connected to weak grids," *IEEE Transactions on Power Systems*, vol. 30, no. 6, pp. 3072–3081, 2015.

[17] Y. Li, L. Fan, and Z. Miao, "Stability control for wind in weak grids," *IEEE Transactions on Sustainable Energy*, vol. 10, no. 4, pp. 2094–2103, 2018.

[18] G. Wu, H. Sun, B. Zhao, S. Xu, X. Zhang, A. Egea-Àlvarez, S. Wang, G. Li, Y. Li, and X. Zhou, "Low-frequency converter-driven oscillations in weak grids: Explanation and damping improvement," *IEEE Transactions on Power Systems*, vol. 36, no. 6, pp. 5944–5947, 2021.

[19] A. Yazdani and R. Iravani, *Voltage-sourced converters in power systems: modeling, control, and applications*. John Wiley & Sons, 2010.

[20] L. Fan, *Control and dynamics in power systems and microgrids*. CRC Press, 2017.

[21] L. Fan and Z. Miao, "An explanation of oscillations due to wind power plants weak grid interconnection," *IEEE Transactions on Sustainable Energy*, vol. 9, no. 1, pp. 488–490, 2018.

[22] Y. Li, L. Fan, Y. Zhou, and Z. Miao, "Stability enhancement module for grid-following converters: Hardware implementation and validation," *International Transactions on Electrical Energy Systems*, vol. 31, no. 11, p. e13115, 2021.

[23] D. Ramasubramanian, W. Baker, J. Matevosyan, S. Pant, and S. Achilles, "Asking for fast terminal voltage control in grid following plants could provide benefits of grid forming behavior," *IET Generation, Transmission & Distribution*, 2022.

[24] B. Badrzadeh, N. Modi, N. Crooks, and A. Jalali, "Power system operation with reduced system strength for inverter-connected generation during prior outage conditions," *CIGRE SCIENCE & ENGINEERING*, vol. 17, pp. 141–149, 2020.

[25] A. Jalali, B. Badrzadeh, J. Lu, N. Modi, and M. Gordon, "System strength challenges and solutions developed for a remote area of australian power system with high penetration of inverter-based resources," *CIGRE SCIENCE & ENGINEERING*, vol. 20, pp. 27–37, Feb 2021.

[26] L. Fan, Z. Miao, and S. Shah, "Mechanism analysis of wind turbine var oscillations," *IEEE Transactions on Industrial Electronics*, pp. 1–4, 2022.

[27] L. Fan, Z. Miao, S. Shah, P. Koralewicz, and V. Gevorgian, "Solar PV and BESS plant-level voltage control and interactions: Experiments and analysis," *IEEE Transactions on Energy Conversion*, pp. 1–10, 2023.

[28] R. Mittal and Z. Miao, 'Linear Time-Periodic Modeling of Single-Phase Elementary Phase-Locked-Loop," *2020 52nd North American Power Symposium (NAPS)*, Tempe, AZ, USA, 2021, pp. 1-6.

[29] R. Mittal, L. Fan and Z. Miao, "Harmonic State-Space Model of Second-Order Generalized Integrator Phase-Locked Loop," *2021 IEEE Power & Energy Society General Meeting (PESGM)*, Washington, DC, USA, 2021, pp. 1-5.

[30] D. Ramasubramanian, E. Farantatos, O. Ajala, S. Dhople, and B. Johnson, "A universal grid-forming inverter model and simulation-based characterization across timescales," in *56th Annual Hawaii International Conference on System Sciences, HICSS 2023*. IEEE Computer Society, 2023, pp. 2631–2640.

[31] L. Fan and Z. Miao, *Modeling and Stability Analysis of Inverter-Based Resources*. CRC Press, 2023.

Ratik Mittal (S'18) was born in Kashipur, India. He received his B.E degree in Electrical Engineering from Thapar University, Patiala, Punjab, in 2015, and the M.S. degree in electrical engineering from the University of South Florida, Tampa Florida, in 2019. He is currently working towards the Ph.D. degree with the Smart Grid Power Systems Lab at the University of South Florida, Tampa Florida. His research interests include power electronics-based power systems modeling and analysis.

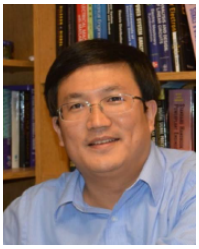

Zhixin Miao (SM'09) received the B.S.E.E. degree from the Huazhong University of Science and Technology,Wuhan, China, in 1992, the M.S.E.E. degree from the Graduate School, Nanjing Automation Research Institute (Nanjing, China) in 1997, and the Ph.D. degree in electrical engineering from West Virginia University, Morgantown, in 2002.

Currently, he is a full professor at University of South Florida (USF), Tampa. Prior to joining USF in 2009, he was with the Transmission Asset Management Department with Midwest ISO, St. Paul, MN, from 2002 to 2009. His research interests include power system real-time simulation, microgrids, and protection. He serves as an associate editor for IEEE transactions on Sustainable Energy.

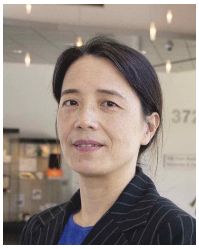

Lingling Fan (SM'08-F'22) received the B.S. and M.S. degrees in electrical engineering from Southeast University, Nanjing, China, in 1994 and 1997, respectively, and the Ph.D. degree in electrical engineering from West Virginia University, Morgantown, in 2001. Currently, she is a full professor at the University of South Florida, Tampa, where she has been since 2009. She was with the transmission planning department at Midwest ISO, St. Paul, MN, form 2001 to 2007, and an assistant professor with North Dakota State University, Fargo, from 2007 to 2009. Her research interests include dynamics, control, and optimization with applications in power systems and power electronics. Dr. Fan serves as the editor-in-chief for IEEE Electrification Magazine and associate editor for IEEE transactions of Energy Conversion.